Supplementary Information

Ultrawide Linear Range, High Sensitivity, and Large-Area Pressure Sensor Arrays Enabled by Pneumatic Spraying Broccoli-Like Microstructures

Zonglin Li,[abc] Kun Li,[abc] Weiwei Wang,[abc] Tong Zhang,*[abd] and Xiaoniu Yang*[abc]

a. State Key Laboratory of Polymer Physics and Chemistry, Changchun Institute of Applied Chemistry, Chinese Academy of Sciences, Changchun 130022, China, E-mail: tzhang@ciac.ac.cn, xnyang@ciac.ac.cn.
b. School of Applied Chemistry and Engineering, University of Science and Technology of China, Hefei 230026, China
c. CAS Key Laboratory of High-Performance Synthetic Rubber and its Composite Materials, Changchun Institute of Applied Chemistry, Chinese Academy of Sciences, Changchun 130022, China
d. Huangpu Institute of Materials, Changchun Institute of Applied Chemistry, Chinese Academy of Science, Guangzhou 510530, China

Keywords**:** flexible pressure sensor; large-area array; pneumatic spraying; ultrawide linear range

This Supplementary Information contains two Supplementary Notes, eleven Supplementary Figures, three Supplementary Tables, and one Supplementary Movie.

Note S1. The calculation of pressure sensor errors

The test method of the performances is basically based on GB/T 15478-2015. There are 11 calibrated points selected from the whole linear range of PSMF-B which are 0, 1, 2, ... 10 MPa. The test contains five loading-unloading cycles and correspond current is collected.

The loading average:

$$\bar{Y}_{U_i} = \frac{1}{n}\sum_{j=1}^{n} Y_{U_{ij}} \quad (1)$$

The unloading average:

$$\bar{Y}_{D_i} = \frac{1}{n}\sum_{j=1}^{n} Y_{D_{ij}} \quad (2)$$

The total average:

$$\bar{Y}_i = \frac{1}{2}(\bar{Y}_{U_i} + \bar{Y}_{D_i}) \quad (3)$$

Where:

$Y_{U_{ij}}$ —— The jth reading of the i-th calibration point of the loading (i=1,2,3, ... 11; j=1,2,3,4,5);

$Y_{D_{ij}}$ —— The jth reading of the i-th calibration point of the unloading (i=1,2,3, ... 11; j=1,2,3,4,5);

n —— The number of repeated experiments.

1) Nonlinear error ξ_L

$$\xi_L = \frac{\left|\bar{Y}_i - Y_i\right|_{max}}{Y_{FS}} \times 100\% \quad (4)$$

Where:

$\bar{Y}_i$ —— The total average calculated by (3);

Y_i —— Response value at calibrate points calculated by the fitting (fitting is conducted in Origin);

Y_{FS} —— Full scale output calculated by the fitting.

2) Hysteresis error ξ_H

$$\xi_H = \frac{\left|\bar{Y}_{U_i} - \bar{Y}_{D_i}\right|_{max}}{Y_{FS}} \times 100\% \quad (5)$$

Where:

$\bar{Y}_{U_i}$, $\bar{Y}_{D_i}$ —— The average of the loading and unloading readings on the same calibrate point.

3) Repeatability error ξ_R

$$\xi_R = \frac{S_{max}}{Y_{FS}} \times 100\% \quad (6)$$

Where:

S_{max} —— The max standard deviation of the 11 calibrate points.

Note S2. Model & calculation for flexible pressure sensors' conducting path

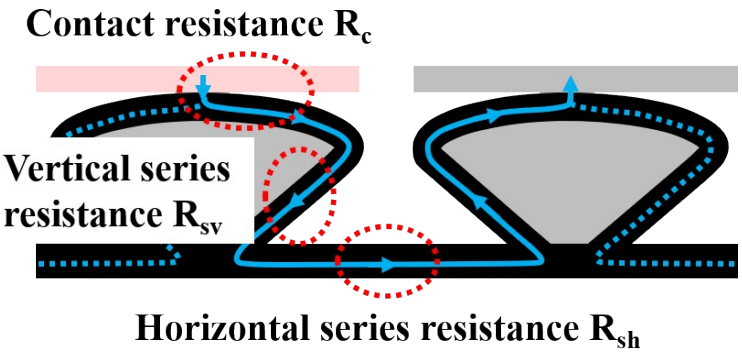

The calculation of R_t is based on the actual testing of each component. Based on the structure of IDE (10 fingers, for each finger 5000 μm length, 400 μm width, and 100 μm gap), we assume that the conductive path mainly formed between the adjacent electrodes. The total resistance contains contact resistance (R_c), vertical series resistance (R_{sv}), and horizontal series resistance (R_{sh}).

$$R_t = R_c + R_{sv} + R_{sh}$$

The contact resistors are parallel, so R_c is considered to be inversely proportional to the contact area. Besides, R_c of fixed area declines with pressure which may result from small roughness of conductive layer and iron plate.

R_{sv} test is shown in Fig. S11. The whole R_{sv} is considered as single R_{sv} of single broccolis parallel together. Meanwhile, broccolis under pressure is assumed proportional to the contact area. So, the total R_{sv} of the sensor can be calculated.

R_{sh} was deduced by the test which depicted in Fig. 5g considering the physical dimension.

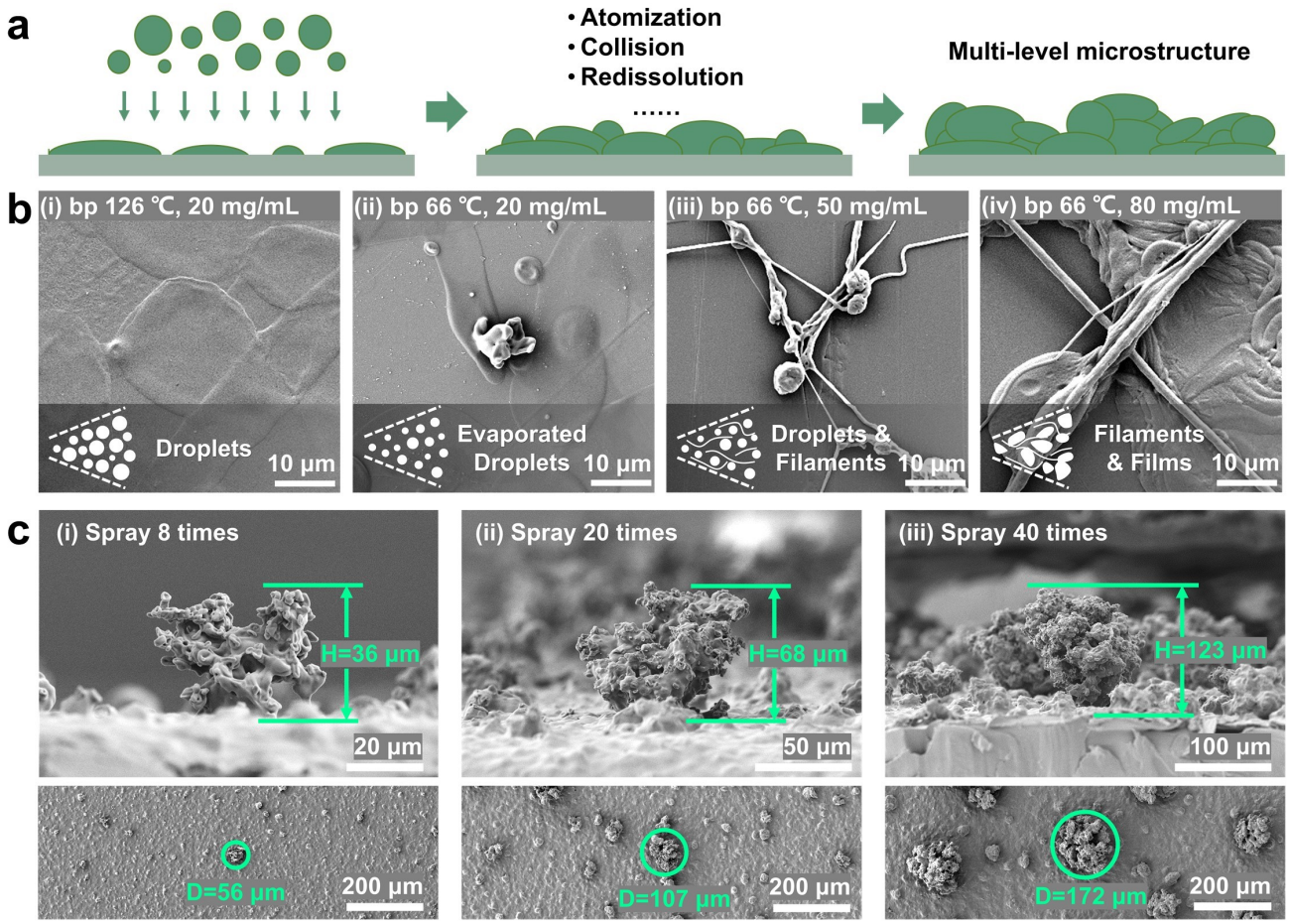

Fig. S1. The formation of pneumatic spraying microstructures. (a) Schematic of microstructure formed by droplet deposition. (b) Various droplet dispersion states controlled by spraying process parameters. (c) The side and top views of microstructures with different spraying times (20 mg/mL, THF).

As mentioned before, the droplets atomized by spray gun will deposit on the substrate, and forming multi-level microstructures as shown in Fig. S1a. Interestingly, there are many factors may affect the spray coated morphology, such as solution atomization status, droplets collision, redissolution after stacking etc. In this work, it is found that boiling point (bp) and solution viscosity can be vital to the formation of pneumatic spraying microstructures. As is shown in Fig. S1b-i, a flattening deposition pattern is obtained in high boiling point solvent system (butyl acetate, bp 126 ℃) because of the atomized droplets will evaporate little solvent during the flight thus still have good fluidity when hitting on the substrate. When using tetrahydrofuran (THF, bp 66 ℃) as solvent, droplets will lose more solvent in the flight period and protruding morphology is obtained (Fig. S1b-ii).

Otherwise, higher viscosity will be adverse to the atomizing of solution into small droplets. As shown in Fig. S1b-iii and iv, filaments and liquid films appear when the concentration is increased. The formation of microstructures based on 20 mg/mL styrene ethylene butylene styrene (SEBS) in THF is further explored in a dynamic perspective by repeating spraying 8, 20, and 40 times as shown in Fig. S1c. In the view of side and top, the particles have grown taller and thicker as the spraying goes on. Based on the above findings, a rational assumption is proposed that the final spraying microstructure morphologies are mainly determined by the solution scatter states which can be diversified by controlling spraying parameters.

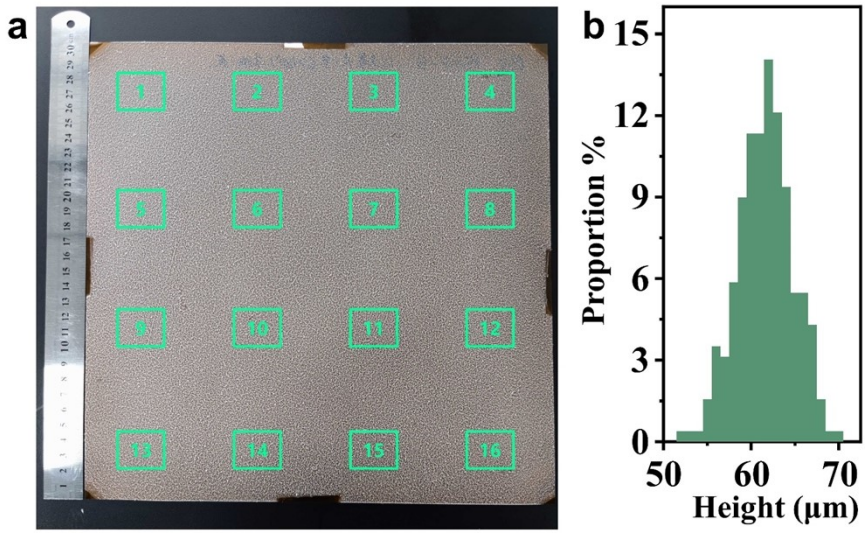

Fig. S2. Uniformity of the 3D surface morphology by measuring the arithmetic mean height of various parts of the fabricated large scale film. (a) a 30*30 cm^2 PSMF-B film and 16 constituencies. (b) Height distribution of PSMF.

Every constituency is divided into 16 little regions. For every region, there is a corresponding arithmetic mean height (σSa) obtained. The average σSa of the 16 little regions is considered as the height of the constituency as shown in Fig. 1a-iii. Fig. S2b shows the distribution of all of the 256 measured points.

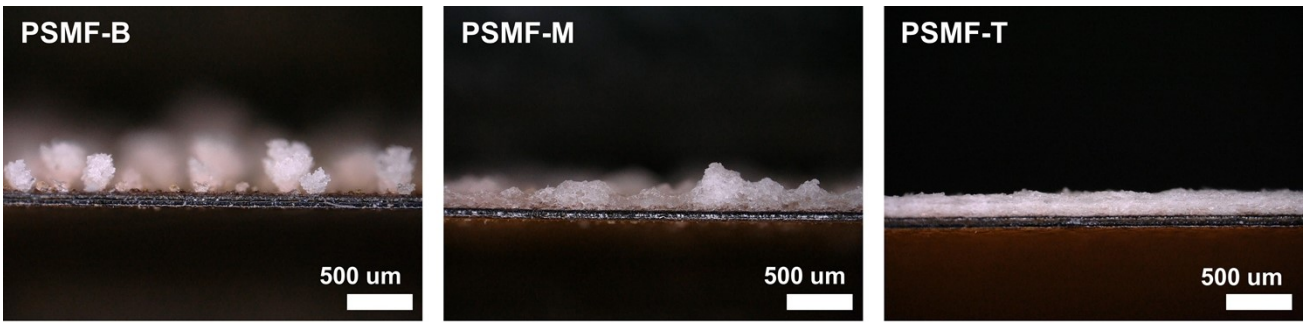

Fig. S3. Optical microscope images of PSMFs from the side view.

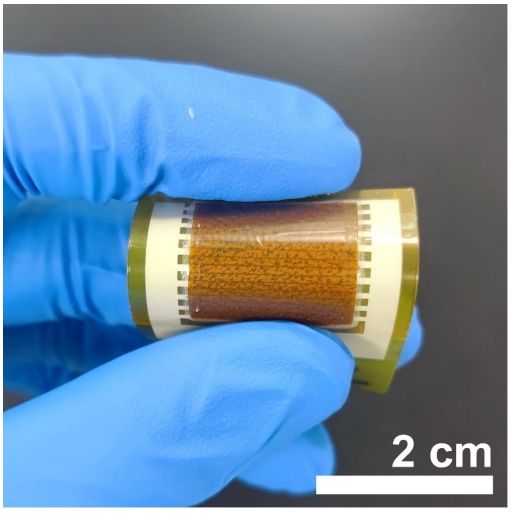

Fig. S4. Photo of the flexible pressure sensor based on PSMF-B.

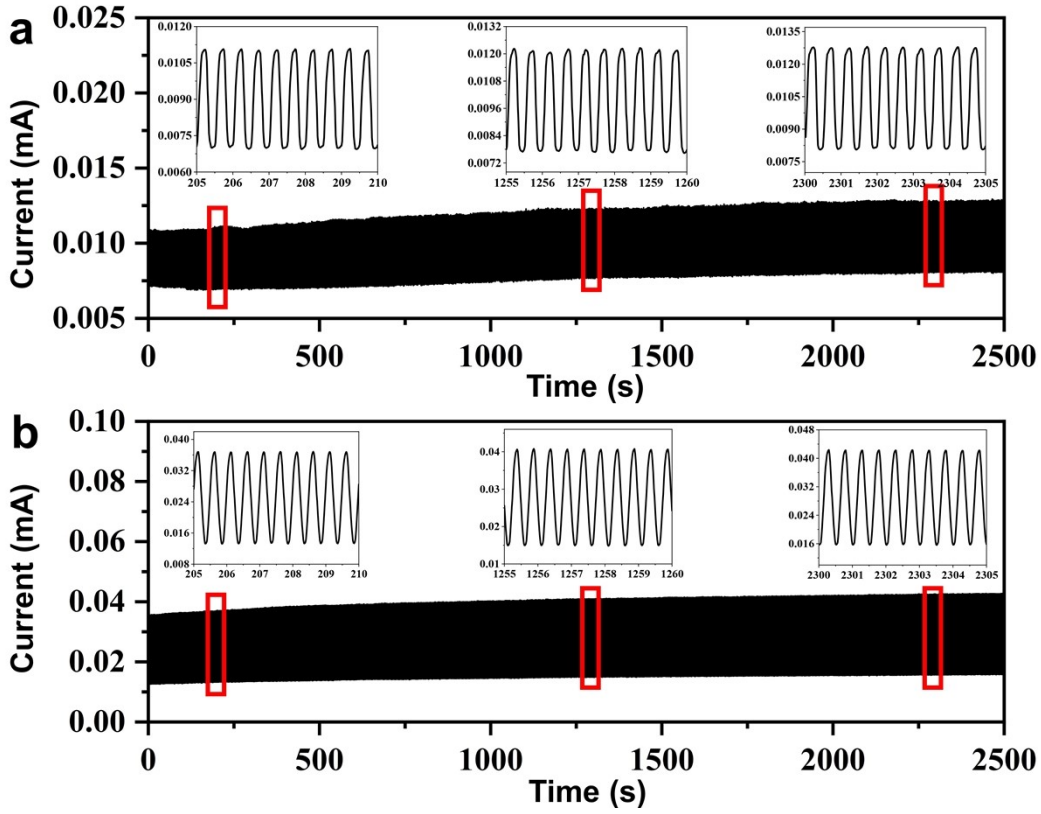

Fig. S5. 5 000 cycles fatigue test of PSMF-B sensor under the pressure of (a) 10-100 kPa, and (b) 100-1 000 kPa. Inset images are the enlarged 10 waves of different time periods marked by red box.

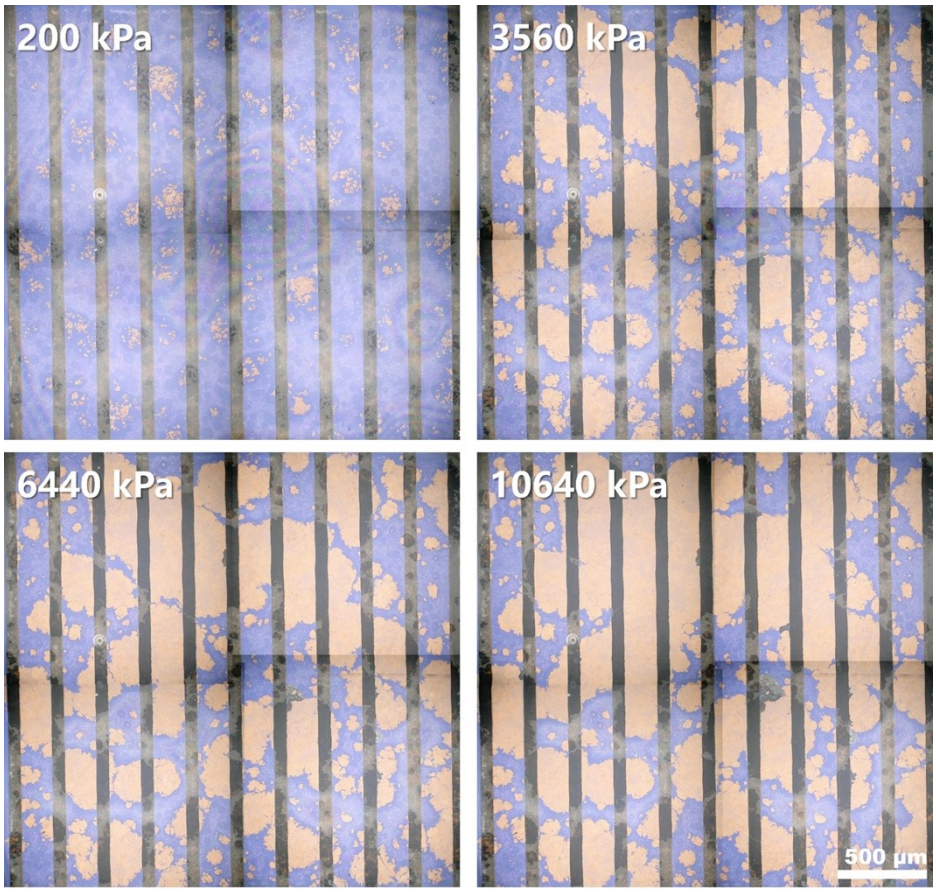

Fig. S6. Optical images of PSMF-B real contacted region with ITO@PET interdigital electrode under different pressures.

The golden area is the contact area. The uncolored narrow strips are non-conductive area where ITO has been etched by laser, and it is difficult to determine whether contact or not due to the color of this part is blurred without ITO reflection. So, no statistics have been made in these strips.

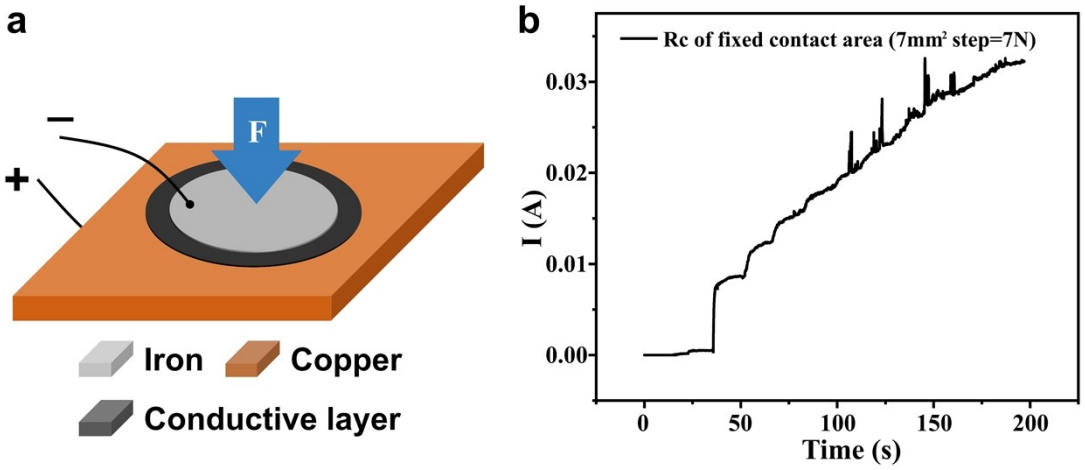

Fig. S7. Contact resistance of a fixed area with an iron plate and conductive layer on smooth copper foil. (a) Schematic of the test and (b) corresponding data.

In this test, the conductive layer is spraying coated on a smooth copper foil and pressed by a circular iron sheet with diameter of 3 mm. A constant voltage of 1 V is applied between the copper foil and iron sheet. As pressure increases, the current increased either. The actual contact interface contains lots of asperity contact regions due to the surface roughness. These contact regions may enlarge under pressing, which causes the varying resistance.

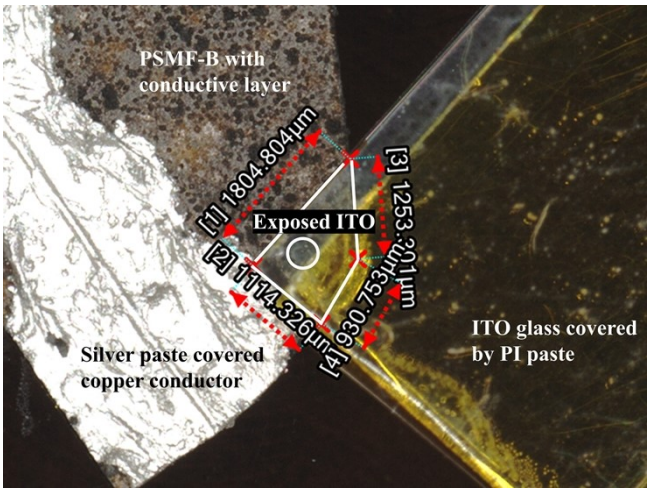

Fig. S8. Optical image of R_{sv} test. The compressed trapezoid like area is about 1.5 mm^2.

In this test, the ITO@glass electrode is laser etched into a ~200 μm wide strip. Then, the ITO strip is covered by an insulating PI paste but expose a small spot. The exposed spot is pressed on a single “broccoli” whose surrounding area have been cleaned to ensure the ITO spot can fully contact with it. On the conductive surface of PSMF-B, the current is collected by a silver paste covered copper conductor. The silver paste is smeared as close as possible to the “broccoli” to reduce the series resistance.

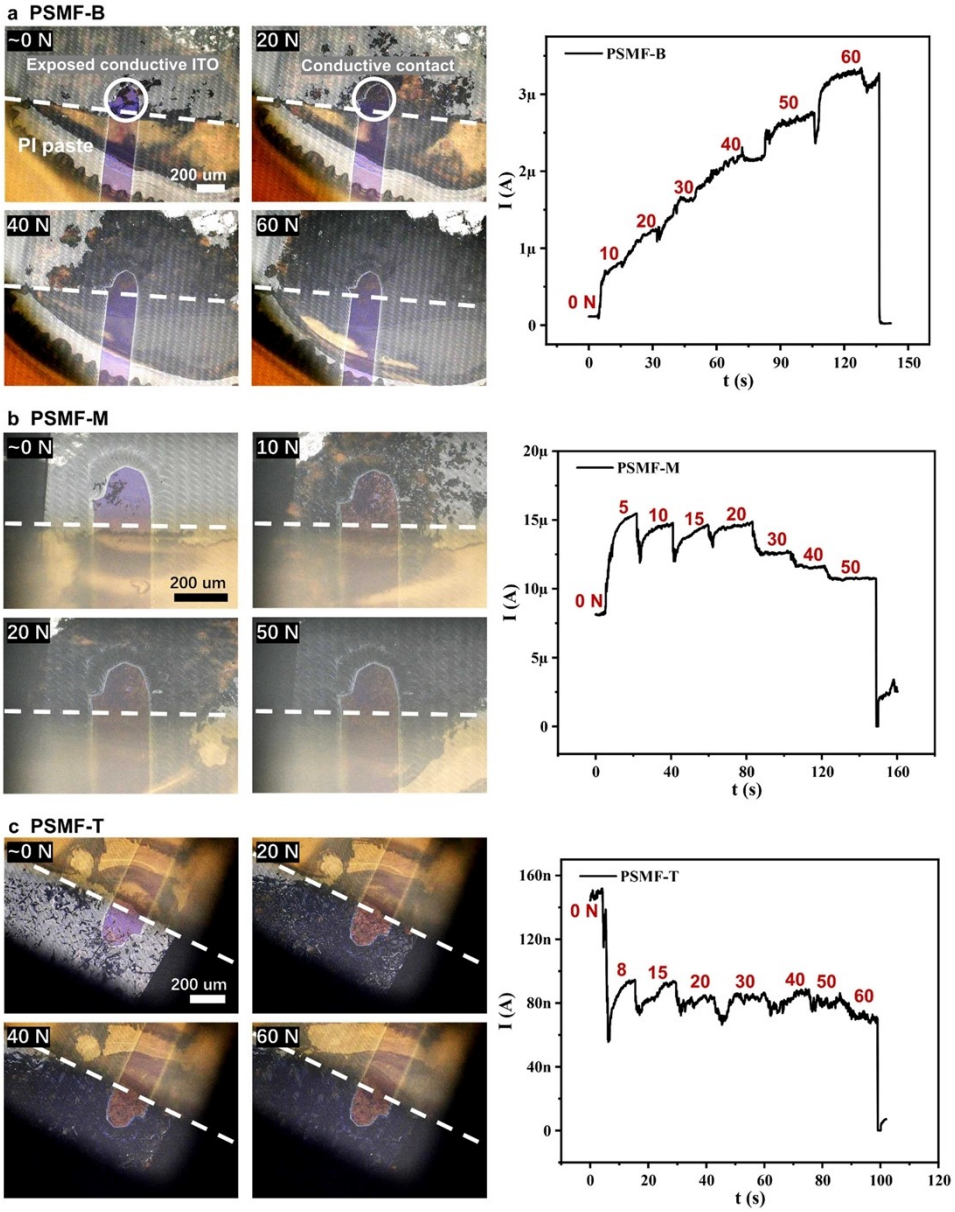

Fig. S9. The in-situ observation optical images of R_{sv} test and corresponding resistance of PSMF-B, PSMF-M, and PSMF-T.

The current of PSMF-B is still increasing after the contact area between ITO spot and the conductive film is saturated (~10 N). However, in the situation of PSMF-M, and PSMF-T, the current is almost unchanged but fluctuate when loading. As for the reduced current (increased resistance), we assume the reason is the crack of conductive layer under large pressure.

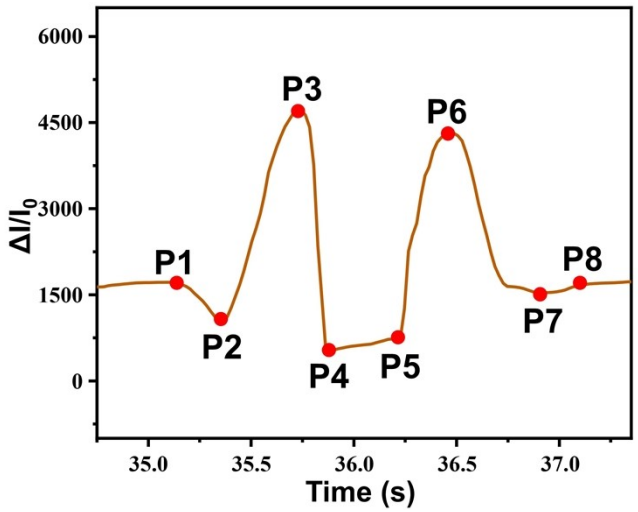

Fig. S10. Single waveform of PSMF-B sensor attached under forefoot when jumping.

Before jumping, we have to stretch the leg muscles and lower the gravity center of the torso that a downward acceleration is required. Then, an upward force is generated from zero to a maximum value and zero to push the body up, and a much higher pressure is detected. When both feet leave the ground, the sensor is only subjected to the pressure from tape fixation that less than standing. The landing process is similarly. Thus, signal during jumping is a more complex bimodal.

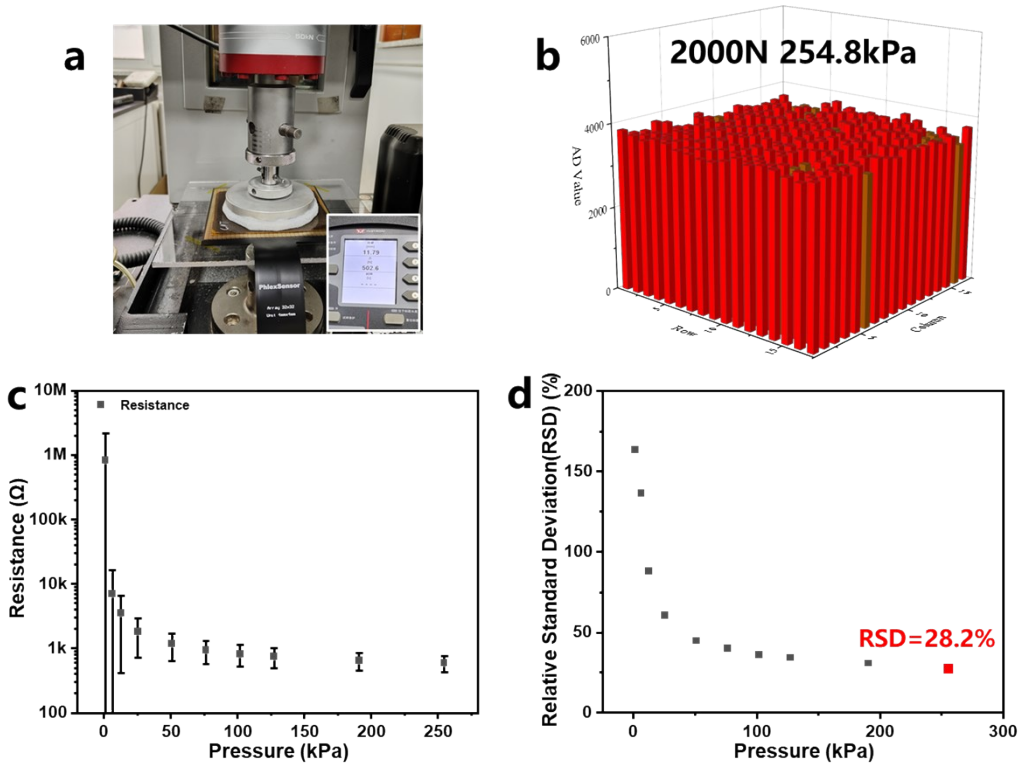

Fig. S11. The uniformity of different sensor units in sensor array. (a) the photo of sensor array uniformity test; (b) the output AD value of 17*17 sensor units under the pressure of 254.8 kPa; (c) the average resistance of 289 pressure sensors under various loading; (d) the calculated RSD.

The performance uniformity of different sensor array units was evaluated by applying pressure by a metal disc of 100 mm diameter as shown in Fig. S11a. The size of a single unit is 4*4 mm^2, and 289 (17*17) units are taken into the relative standard deviation (RSD) count (Fig. S11b) (RSD is a commonly used indicator to evaluate the uniformity). As shown in Fig. S11c, and S11d, the uniformity is poor in the low pressure range, that may cause by some unstably contact units. With the pressure increases, the uniformity gets better and the lowest RSD is 28.2% (@254.8 kPa).

Table S1. The numerical characteristics of PSMFs in a certain area (7.56 mm*5.6 mm).

Unit	Sa [μm]	Sz [μm]	Spc [mm^{-1}]	Sdr
PSMF-B	82	574	79.2	1.34
PSMF-M	48	368	30.3	0.21
PSMF-T	11	112	14.8	0.02

Sa (Arithmetical Mean Height). It expresses, as an absolute value, the difference in height of each point compared to the arithmetical mean of the surface. This parameter is used generally to evaluate surface roughness.

Sz (Maximum Height) is defined as the sum of the largest peak height value and the largest pit depth value within the defined area.

Spc (arithmetic mean peak curvature). Spc represents the arithmetic mean of the principal curvature of the peaks on the surface. A smaller value indicates that the points of contact with other objects have rounded shapes; a larger value indicates that the points of contact with other objects have pointed shapes.

Sdr (Developed Interfacial Area Ratio). This parameter is expressed as the percentage of the definition area's additional surface area contributed by the texture as compared to the planar definition area.

Refer to: Keyence, Area roughness parameters, https://www.keyence.com/ss/products/microscope/roughness/surface/parameters.jsp

Table S2. Comparison of sensing performances of previous pressure sensors in terms of sensing principle, microstructure fabrication method, linear range, sensitivity, and limit of detection.

Sensing Principle	Microstructure fabrication method	Linear Range [kPa]	Sensitivity [kPa^{-1}]	LR*S	Limit of Detection [Pa]	Ref.
Piezoresistive	Transfer micro-dome	353	47.7	16 838.1	1.3	[1]
	Transfer pyramid-like sub-microstructure	300	133	39 900	-	[4]
	Transfer micropyramid	200	18.94	3 788	-	[6]
	Electrospinning PI film	45 000	0.03866	1 739.7	8.2	[17]
	Transfer mesh	1 000	20.9	20 900	7.4	[32]
	Transfer pyramid-wall grid	1.6	383 665.9	613 865.44	5	[33]
	3D-printing inclined-tip	400	212	84 800	7.69	[34]
	CNT-coated sugar created dual-scale pores	4 000	74.5	298 000	40	[35]
	Electrospinning PEI film	40	156	6240	9	[36]
	Freeze dried TPU foam	1 940	0.00152	2.9488	-	[37]
Capacitance (EDL)	Transfer sandpaper	2 000	9.17	18 340	13	[38]
	Transfer graded interlock micro-dome	500	49.4	24 700	-	[39]
	Transfer sandpaper	360	229.9	82 764	0.08	[40]

	Transfer cup-shaped microcolumns	170	87.75	14 917.5	0.7	[41]
	Electrospinning and transfer	100	9029	902 900	5	[42]
	Transfer Calathea zebrina leaf	90	37.8	3402	24	[43]
	Commercial melamine foam	300	1126.96	338 088	1.9	[44]
	Transfer sandpaper	450	810	364 500	-	[45]
Capacitance	Porous GO foam	4	0.8	3.2	0.24	[46]
	UV digital lithography micropillars	10	2.3	23	-	[47]
	Inkjet print micro-dome	10	10.4	104	-	[48]
	Drop-casted silver nanowire mesh	7	0.124	0.868	2	[49]
	Transfer porous pyramid	35	44.5	1 557.5	0.14	[50]
	Customized nylon netting	5	0.33	1.65	3.3	[51]
	Stretch-etch-release PDMS micro-array	9	2.04	18.36	7	[52]
	PDMS foam by etching Ni skeleton	500	2.155	1 077.5	50	[53]
Piezoresistive	Pneumatic Spraying	10 000	98.71	987 100	5	This Work

Table S3. The original data of repeatability test.

Pressure/MPa	Current/mA						
	Cycle 1	Cycle 2	Cycle 3	Cycle 4	Cycle 5	Average	yEr±
0	6.40E-04	6.76E-04	6.02E-04	5.98E-04	7.60E-04	6.55E-04	6.66E-05
1	0.0187	0.0192	0.0193	0.0205	0.0209	0.01972	9.34E-04
2	0.039	0.0394	0.04	0.0414	0.0419	0.04034	0.00126
3	0.0587	0.0566	0.0572	0.0592	0.0608	0.0585	0.00167
4	0.0789	0.0764	0.0768	0.0795	0.0795	0.07822	0.00151
5	0.0972	0.0936	0.0939	0.0972	0.0984	0.09606	0.00217
6	0.117	0.113	0.113	0.116	0.116	0.115	0.00187
7	0.134	0.131	0.13	0.132	0.133	0.132	0.00158
8	0.15	0.146	0.146	0.15	0.151	0.1486	0.00241
9	0.165	0.163	0.163	0.167	0.167	0.165	0.002
10	0.1806	0.17694	0.17993	0.18372	0.18352	0.18094	0.00281

Supplementary Movie S1. The spraying process of the self-built three axis automatic spraying device.